

Two-component jet model for multiwavelength afterglow emission of the extremely energetic burst GRB 221009A

Yuri Sato^{1*}, Kohta Murase^{2,3,4,5,6}, Yutaka Ohira⁷ and Ryo Yamazaki^{1,8}

¹*Department of Physical Sciences, Aoyama Gakuin University, 5-10-1 Fuchinobe, Sagami-hara 252-5258, Japan*

²*Department of Physics, Pennsylvania State University, University Park, Pennsylvania 16802, USA*

³*Department of Astronomy & Astrophysics, Pennsylvania State University, University Park, Pennsylvania 16802, USA*

⁴*Center for Multimessenger Astrophysics, Pennsylvania State University, University Park, Pennsylvania 16802, USA*

⁵*School of Natural Sciences, Institute for Advanced Study, Princeton, NJ 08540, USA*

⁶*Center for Gravitational Physics and Quantum Information, Yukawa Institute for Theoretical Physics, Kyoto University, Kyoto, Kyoto 606-8502, Japan*

⁷*Department of Earth and Planetary Science, The University of Tokyo, 7-3-1 Hongo, Bunkyo-ku, Tokyo 113-0033, Japan,*

⁸*Institute of Laser Engineering, Osaka University, 2-6 Yamadaoka, Suita, Osaka 565-0871, Japan*

26 April 2023

ABSTRACT

Recently gamma-ray bursts (GRBs) have been detected at very high-energy (VHE) gamma-rays by imaging atmospheric Cherenkov telescopes, and a two-component jet model has often been invoked to explain multiwavelength data. In this work, multiwavelength afterglow emission from an extremely bright GRB, GRB 221009A, is examined. The isotropic-equivalent gamma-ray energy of this event is among the largest, which suggests that similarly to previous VHE GRBs, the jet opening angle is so small that the collimation-corrected gamma-ray energy is nominal. Afterglow emission from such a narrow jet decays too rapidly, especially if the jet propagates into uniform circumburst material. In the two-component jet model, another wide jet component with a smaller Lorentz factor dominates late-time afterglow emission, and we show that multiwavelength data of GRB 221009A can be explained by narrow and wide jets with opening angles similar to those employed for other VHE GRBs. We also discuss how model degeneracies can be disentangled with observations.

Key words: radiation mechanisms: non-thermal — gamma-ray bursts: individual: GRB 221009A.

1 INTRODUCTION

In recent years, very-high-energy (VHE) gamma-ray photons from some gamma-ray bursts (GRBs) have been detected (MAGIC Collaboration et al. 2019a,b; Abdalla et al. 2019; Blanch et al. 2020; H.E.S.S. Collaboration et al. 2021). The observed VHE gamma-ray emission is difficult to explain only with synchrotron radiation, and several alternative processes have been proposed, such as synchrotron self-Compton (SSC), external inverse-Compton, proton synchrotron, and proton-induced cascade emissions (e.g., Nava 2021; Gill & Granot 2022). VHE gamma-ray observations will bring us new information on the physical mechanisms of GRBs, including both dynamics and particle acceleration and they can be used for testing fundamental physics.

GRB 221009A was an extremely energetic event. With its redshift of 0.1505 (Castro-Tirado et al. 2022), the isotropic-equivalent gamma-ray energy is at least $E_{\text{iso},\gamma} \approx$

$1.0\text{--}1.2 \times 10^{55}$ erg (Frederiks et al. 2023; Burns et al. 2023). The *Fermi* Large Area Telescope reported high-energy (HE: 0.1–10 GeV) gamma-ray photons, and the highest-energy photon reached around 100 GeV (Pillera et al. 2022). The Large High Altitude Air Shower Observatory (LHAASO) detected more than 5000 VHE gamma-ray photons above 500 GeV within 2000 s after the GBM trigger, and the highest photon energy reached ≈ 18 TeV (Huang et al. 2022). The HE and VHE gamma-ray light curves may be affected by the $\gamma\gamma$ annihilation with source photons (Murase et al. 2022; Zhang et al. 2022) and the extragalactic background light (EBL; e.g., Murase et al. 2007). These observations could also provide constraints on the model parameters such as the radiation region, the bulk Lorentz factor, and the jet opening angle.

Multiwavelength afterglow emission of GRB 221009A has been observed in HE gamma-ray, X-ray, optical, and radio bands (e.g., Fulton et al. 2023; Williams et al. 2023; Shrestha et al. 2023; Laskar et al. 2023; Kann et al. 2023; Levan et al. 2023). The X-ray and optical luminosities

* E-mail: yuris@phys.aoyama.ac.jp (YS)

ties are much brighter than those of typical long GRBs (Ror et al. 2022), while the radio (15 GHz) luminosity ($\approx 1 \times 10^{29}$ erg s $^{-1}$ Hz $^{-1}$ at 10 days) is lower than typical long GRBs including VHE gamma-ray event [e.g., $\approx 4 \times 10^{30}$ erg s $^{-1}$ Hz $^{-1}$ for GRB 180720B (Rhodes et al. 2020)]. Furthermore, around 4×10^4 s, the High-Altitude Water Cherenkov Observatory obtained the flux upper limit (Ayala et al. 2022), which is converted to the luminosity of $\approx 1 \times 10^{18}$ erg s $^{-1}$ Hz $^{-1}$ at 1 TeV. This value is smaller than that of GRB 180720B ($\approx 3 \times 10^{20}$ erg s $^{-1}$ Hz $^{-1}$ at 3.6×10^4 s), and it is almost comparable to that of GRB 190829A ($\approx 3 \times 10^{17}$ erg s $^{-1}$ Hz $^{-1}$ at 2.7×10^4 s). These properties of the observed afterglow emission give us constraints on the modeling. A possible interpretation for GRB 221009A is that a uniform jet propagates into a wind medium (Ren, Wang, & Zhang 2022).

In this Letter, to explain multiwavelength afterglow emission of GRB 221009A, we consider a two-component jet model, in which two top-hat jets with different opening angles propagating into uniform interstellar medium (ISM; e.g., Ramirez-Ruiz, Celotti, & Rees 2002; Berger et al. 2003; Huang et al. 2004; Peng, Königl, & Granot 2005; Wu et al. 2005; Racusin et al. 2008; Sato et al. 2021, 2023; Rhodes et al. 2022). GRB 221009A is among bursts with the largest $E_{\text{iso},\gamma}$ (e.g., Atteia et al. 2017; Zhao et al. 2020). This suggests that the GRB jet has a small initial opening half-angle θ_0 so that we get a normal value of the collimation-corrected gamma-ray energy, $E_\gamma = E_{\text{iso},\gamma} \theta_0^2 / 2 \sim 10^{50}$ erg (see Figure 1 of Zhao et al. 2020). For example, if we take a typical value, $\theta_0 \approx 0.1$ rad, then we get an extremely large value, $E_\gamma \approx 5 \times 10^{52}$ erg (e.g., Zhao et al. 2020). However, due to the jet break effect, afterglow emission from a jet with a small opening angle decays more rapidly than observed. With another less collimated jet component, late-time afterglow emission can be as bright as observed (Sato et al. 2021, 2023). Furthermore, we investigate the detectability of SSC photons with $\mathcal{O}(10)$ TeV. In this Letter, cosmological parameters, $H_0 = 71$ km s $^{-1}$ Mpc $^{-1}$, $\Omega_M = 0.27$ and $\Omega_\Lambda = 0.73$ are adopted.

2 MODEL DESCRIPTION

In this Letter, we consider the two-component jet model, in which the overall flux is simply given by a superposition of emission from two relativistically moving top-hat jets. Here, we shortly summarize the calculation of the emission from a single top-hat jet (see Huang et al. 2000, for details). Taking into account the radiative losses, we calculate the dynamics of the jet (that is characterized only by the evolution of the shock radius, the bulk Lorentz factor, and the jet opening half-angle) and resulting multiwavelengths afterglow emission. Unless otherwise stated, it is assumed that the jet propagates into the uniform surrounding material, that is, the ISM with constant density n_0 . The jet is assumed to have the isotropic-equivalent kinetic energy $E_{\text{iso,K}}$, the bulk Lorentz factor Γ_0 , and the opening half-angle θ_0 . We also assume a power-law electron energy distribution with a spectral index p , and constant microphysics parameters ϵ_e , ϵ_B , and f_e , which are the energy fractions of the internal energy going into non-thermal electrons, magnetic fields, and the number fraction of

accelerated electrons, respectively. Then, the synchrotron and SSC emissions are numerically computed taking into account the Klein-Nishina effect (e.g., Nakar, Ando, & Sari 2009; Murase et al. 2010, 2011; Wang et al. 2010; Zhang et al. 2021; Jacovich, Beniamini, & van der Horst 2021; Sato et al. 2023). The EBL absorbs the VHE gamma-ray photons. We calculate the EBL absorption following Franceschini, Rodighiero, & Vaccari (2008) by using the PYTHON package ‘EBL table’¹. The flux density F_ν is obtained by integrating the emissivity along the equal arrival time surface (e.g., Granot, Piran, & Sari 1999). GRB 221009A was so bright that the viewing angle, which is the angle between the jet axis and the observer’s line of sight, can be taken as $\theta_v = 0$.

3 RESULTS OF AFTERGLOW MODELING

In this section, we show our numerical results of multiwavelength afterglow emission in VHE gamma-ray (1 TeV), HE gamma-ray (1 GeV), X-ray (1 keV), optical (r band) and radio (1.3, 5.0, 15.8 and 99.9 GHz) bands, and compare them with the observed data of GRB 221009A. The X-ray data are taken from the *Swift* team website² (Evans et al. 2007, 2009). We convert the observed energy flux in 0.3–10 keV to the flux density at 1 keV, assuming that the photon index is 1.8 during slow-cooling epochs. The VHE gamma-ray upper limit is obtained from Ayala et al. (2022). Observed HE gamma-ray flux is taken from Ren, Wang, & Zhang (2022). The observed energy flux in 0.1–10 GeV is converted to the flux density at 1 GeV with the photon index of 1.87 (Pillera et al. 2022). Optical data are extracted from Fulton et al. (2023) and Laskar et al. (2023). We adopt the r -band extinction $A_r = 4.31$ mag (Ren, Wang, & Zhang 2022). Radio data is taken from Laskar et al. (2023).

3.1 One-component jet model

Before going to the two-component jet model, here we discuss the emission from the single top-hat jet model to show that the latter hardly explains the multiwavelength afterglow emission of GRB 221009A. Given that the isotropic energy of the prompt emission $E_{\text{iso},\gamma} \sim 10^{55}$ erg, it is natural to set $E_{\text{iso,K}} \sim 10^{55}$ erg so that the efficiency of the prompt emission, $E_{\text{iso},\gamma} / (E_{\text{iso},\gamma} + E_{\text{iso,K}})$, can be reasonable. Note that the isotropic-equivalent kinetic energy adopted by Ren, Wang, & Zhang (2022) is smaller than ours, in which a very high radiative efficiency is indicated.

First, we consider the jet with a typical initial opening half-angle, $\theta_0 = 0.1$ rad, propagating into a uniform ISM. In order to fit the observed X-ray and r -band light curves, we set model parameters as $\theta_v = 0$, $E_{\text{iso,K}} = 1.0 \times 10^{55}$ erg, $\Gamma_0 = 285$, $n_0 = 1.0 \times 10^{-2}$ cm $^{-3}$, $p = 2.7$, $\epsilon_e = 8.0 \times 10^{-4}$, $\epsilon_B = 4.0 \times 10^{-3}$, and $f_e = 0.1$. The jet with these parameters is referred to as ‘typical jet I’ in the following. Figure 1(a) shows the result. While the jet is in the adiabatic

¹ <https://pypi.org/project/ebhtable/>

² <https://www.swift.ac.uk/xrt.curves/01126853/>

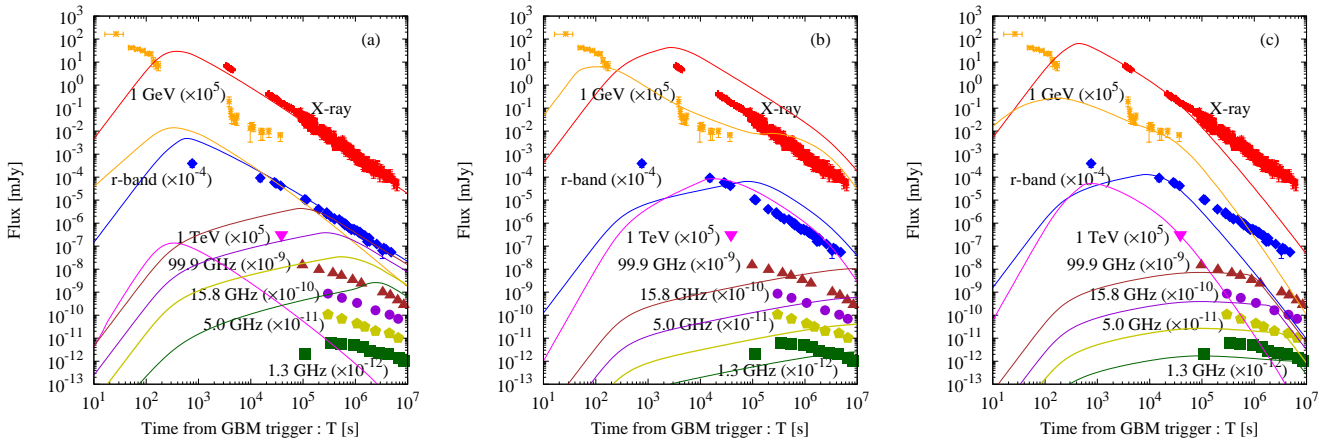


Figure 1. Multiwavelength afterglow light curves of GRB 221009A from models with single top-hat jets. Theoretical results in VHE gamma-ray (1 TeV: magenta), HE gamma-ray (1 GeV: orange), X-ray (1 keV: red), optical (r band: blue) and radio bands (1.3 GHz: green, 5.0 GHz: yellow, 15.8 GHz: violet, and 99.9 GHz: brown) are compared with the observations [1 TeV (upper limit): magenta downward triangle, 1 GeV: orange points, X-ray: red points, r band: blue diamonds, 99.9 GHz: brown upward triangles, 15.8 GHz: violet circles, 5.0 GHz: yellow pentagons and 1.3 GHz: green square]. The solid lines in panels (a), (b) and (c) show the fluxes from the typical jet I, II, and the narrow jet, respectively. All three models have difficulty in explaining the observed data.

deceleration phase, the cooling frequency ν_c , the typical frequency ν_m and the absorption frequency ν_a obey the relation $\nu_a < \nu_m < \nu_c$. The cooling frequency ν_c is between the r band and X-ray bands, and ν_m is lower than the r band. The X-ray and optical light curves follow the scalings $F_\nu \propto T^{(2-3p)/4} \sim T^{-1.5}$ and $F_\nu \propto T^{3(1-p)/4} \sim T^{-1.3}$, respectively (e.g., Gao et al. 2013), which is roughly consistent with the observed data. However, the numerical results in 1.3, 5.0, 15.8 and 99.9 GHz bands are about three orders of magnitude brighter than the observed data (green, yellow, violet, and brown lines in Fig. 1(a)). Moreover, our numerical HE gamma-ray light curve is about an order of magnitude dimmer than the observed HE gamma-ray flux (orange line in Fig. 1(a)). Note that the value of $\epsilon_e/f_e = 8.0 \times 10^{-3}$ is unusually small.

Secondly, we change microphysics parameters to fit the observed dim radio emission. If we take larger ϵ_e , smaller ϵ_B , and/or smaller f_e , then the radio flux becomes small. We adopt $\theta_v = 0$, $\theta_0 = 0.1$ rad, $E_{\text{iso,K}} = 1.0 \times 10^{55}$ erg, $\Gamma_0 = 285$, $n_0 = 1.0 \times 10^{-2}$ cm $^{-3}$, $p = 2.7$, $\epsilon_e = 0.4$, $\epsilon_B = 1.0 \times 10^{-6}$, and $f_e = 0.08$ (we call this ‘typical jet II’). As shown in Fig. 1(b), the radio emission can be dimmer. However, our VHE gamma-ray, HE gamma-ray, X-ray and optical fluxes overpredict the observations. Moreover, our radio fluxes are still inconsistent with the observational results. Therefore, models with typical jets I and II having $\theta_0 = 0.1$ rad are excluded.

Next, we try to explain radio afterglows with another parameter set. Once $E_{\text{iso,K}}$ is large, we need small n_0 and/or θ_0 to have dim radio emission. The observed small radio fluxes require the jet with a small initial opening half-angle (Sato et al. 2021, 2023). Here, we introduce ‘narrow jet’ with $\theta_0 = 0.01$ rad, and we set $\theta_v = 0$, $E_{\text{iso,K}} = 1.0 \times 10^{55}$ erg, $\Gamma_0 = 285$, $n_0 = 1.0 \times 10^{-2}$ cm $^{-3}$, $p = 2.7$, $\epsilon_e = 0.1$, $\epsilon_B = 2.5 \times 10^{-5}$, and $f_e = 0.2$ to fit the HE gamma-ray light curve. It is found from Figure 1(c) that our narrow jet is hard to explain the observed late ($T \gtrsim 3 \times 10^4$ s) X-ray and optical afterglows. The jet break time is given by $T_{\text{jet}} \sim (3E_{\text{iso,K}}/4\pi n_0 m_p c^5)^{1/3} \theta_0^{8/3}$, where m_p is the mass of

the proton and c is the speed of light (Sari, Piran, & Halpern 1999). For our narrow jet, we obtain $T_{\text{jet}} \approx 2.4 \times 10^3$ s. After the jet break, the X-ray and optical fluxes decay much steeper than the observed ones (orange, red, and blue lines in Fig. 1(c)). The initial opening half-angle of the narrow jet is rather small. However, our narrow jet is fat in a sense, $\theta_0 > \Gamma_0^{-1}$.

As shown earlier, the cases of constant ISM hardly explain the observed afterglow emissions. Another possibility is to consider a wind-like circumstellar medium (Ren, Wang, & Zhang 2022). Then, the late X-ray, optical, and radio afterglows are better explained. Even in this case, however, the predicted HE gamma-ray flux after $T \gtrsim 2 \times 10^4$ s is about six times dimmer than the observational result. We tried various parameter sets to fit the data, however, we did not find better combinations than those described earlier for the uniform density case. Hence, it is challenging for the single top-hat jet model to well describe observed multiwavelength afterglow emission. This conclusion is consistent with analysis done by Laskar et al. (2023). In our previous work, ‘two-component jet model’, in which another wider jet is added to the narrow jet component, was required to explain the observed afterglows of the other VHE gamma-ray events reported so far (Sato et al. 2021, 2023). In the next subsection, we will investigate whether GRB 221009A can be described by the same model.

3.2 Two-component jet model

In this subsection, we show the result of our two-component jet model, in which another ‘wide jet’ emission is introduced in addition to the narrow jet given in § 3.1. It is assumed that the two jets are on co-axis and ejected from the central engine simultaneously. The observed flux can be described by a superposition of emission components from the two independent jets until $T \sim 1 \times 10^7$ s. This is because the solid angle of the narrow jet is small enough compared with that of the wide jet until $T \sim 1 \times 10^7$ s in our model parameter set. After this time-scale, the expansion of the narrow jet affects

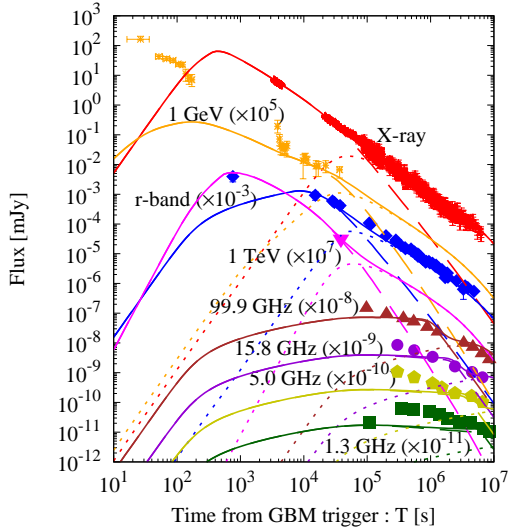


Figure 2. Multiwavelength afterglow light curves calculated by the two-component jet model. The meanings of colors and symbols are the same as in Fig. 1. The solid lines are the sum of the narrow (dashed lines) and wide (dotted lines) jet components.

the dynamics of the wide jet. For the narrow jet, we use the parameters determined in § 3.1. The parameters of the wide jet are $\theta_v = 0$, $\theta_0 = 0.1$ rad, $E_{\text{iso,K}} = 2.0 \times 10^{53}$ erg, $\Gamma_0 = 24$, $n_0 = 1.0 \times 10^{-2}$ cm $^{-3}$, $p = 2.4$, $\epsilon_e = 0.4$, $\epsilon_B = 4.0 \times 10^{-5}$, and $f_e = 0.1$. The constant ISM density is considered in this subsection as well as in § 3.1. The microphysics parameters for the narrow and wide jets have different values, although the differences are small. If the circumburst or ejecta of the narrow and wide jets are different, the two jets may not have common microphysics parameters (Sato et al. 2023). Indeed, some authors have adopted different values of ϵ_e , ϵ_B and f_e for the two jets (e.g., Racusin et al. 2008; Sato et al. 2021, 2023; Rhodes et al. 2022).

As seen in Fig. 2, the narrow jet emission is consistent with the early X-ray and optical data (dashed lines). Moreover, the late X-ray and optical data points are explained by the wide jet emission (dotted lines). At $T \approx 3 \times 10^4$ s, the wide jet enters the adiabatic expansion phase. Subsequently, ν_m intersects the r -band at $T \approx 5 \times 10^4$ s. After that, ν_m is below the r -band and ν_c is between the optical and X-ray bands, so that the X-ray and r -band light curves follow $F_\nu \propto T^{(2-3p)/4} \sim T^{-1.5}$ and $F_\nu \propto T^{3(1-p)/4} \sim T^{-1.3}$, respectively. The late X-ray and r band data are well explained by the wide jet. The electron spectral indices of the narrow jet ($p = 2.7$) are roughly consistent with an observed X-ray photon index of 1.8.

Although the observed HE gamma-ray flux is much brighter than our afterglow model before $T \sim 10^3$ s, such early HE gamma-ray emission may largely originate from inner jets and/or the external reverse shock (Ren, Wang, & Zhang 2022; Zhang et al. 2022). The reverse shock emission could also contribute to the observed flux in the optical band at $T \approx 3 \times 10^3$ s. The optical data may also be prompt optical emission. The numerical radio fluxes are sometimes smaller than the observed ones (brown, violet, yellow and green lines in Figs. 2 and A1 in the online material). The radio emission may be another component (Laskar et al. 2023; O’Connor et al. 2023).

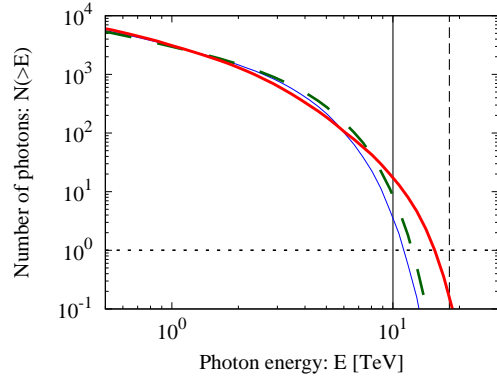


Figure 3. The expected number of VHE photons detected by LHAASO for the narrow jet until 2000 s after the *Fermi*/GBM trigger. The thin-blue-solid (Franceschini, Rodighiero, & Vaccari 2008), thick-green-dashed (Gilmore et al. 2012), and thick-red-solid (Finke, Razzaque, & Dermer 2010) lines are for different EBL models. The vertical black solid and dashed lines represent photon energies (E) of $E = 10$ TeV and 18 TeV, respectively. The horizontal dotted line shows $N(>E) = 1$.

4 SUMMARY AND DISCUSSION

Using a two-component jet model, we have modeled multiwavelength afterglow of GRB 221009A assuming that the ambient matter is homogeneous. We have shown that the observed HE gamma-ray, X-ray and optical afterglows are explained by the sum of the narrow and wide jet components. For our model parameters, the collimation-corrected kinetic energy, $E_{\text{jet,K}} = E_{\text{iso,K}} \theta_0^2 / 2$, of the narrow jet is estimated to be 5.0×10^{50} erg, but it is still about five times larger than the normal value. Our narrow jet may have large values of $E_{\text{iso,K}}$, which are comparable to the observed isotropic-equivalent gamma-ray energy of the prompt emission, $E_{\text{iso},\gamma}$, which is among the largest. However, since its jet opening angle is small, the value of $E_{\text{jet,K}}$ as well as the collimation-corrected gamma-ray energy of the prompt emission can remain normal, making energetics requirements reasonable.

We also evaluate the number of VHE gamma-ray photons, which can be detected by LHAASO. In Fig. 3, we show the result for 2000 s after the *Fermi*/GBM trigger, for the narrow jet (e.g., Zhang et al. 2022). For the EBL absorption, three different models are adopted. The effective areas of the LHAASO Water Cerenkov Detector Array for the zenith angle between 15 and 30 deg and that of the LHAASO larger air shower kilometer square area are obtained from Wang et al. (2022) and Ma et al. (2022), respectively. For our parameter set, the emission radius is so large that the intra-source $\gamma\gamma$ annihilation (Svensson 1987) would not strongly affect the VHE gamma-ray flux (see Section 4.1 in Zhang et al. 2022). Our results indicate that $\gtrsim 500$ GeV gamma-ray photons from the SSC component of the narrow jet could be detected by the LHAASO with a significance level > 100 s.d. in the Li-Ma significance; otherwise the VHE observations can constrain our model.

VHE gamma-ray and radio data could be relevant for discriminating the two-component jet model from the other models. Radio emission from the narrow jet decays rapidly after $T \gtrsim 10^6$ s. The wide jet enhances the radio flux until $T \sim 10^7$ s. In this case, the transition from the narrow to wide jet components may appear as shown in Figs. 2

and A1, which may be used as a test for the existence of the wide jet by radio observations. However, the radio data may also come from another component, e.g., reverse shock (O'Connor et al. 2023), and numerical radio fluxes that are not compatible with the observed radio data reported by Laskar et al. (2023) do not mean that the model is excluded. The early ($T \lesssim 10^3$ s) VHE gamma-ray light curve shows rising both in the constant ISM and in the wind circumburst medium cases. The slope is much shallower in the latter case than in the former (Ren, Wang, & Zhang 2022). The temporal evolution in the rising part in VHE gamma-ray band may become diagnostic to discriminate between the two cases.

Sato et al. (2023) considered the two-component jet model for the other VHE GRBs that were reported previously. They found that all VHE gamma-ray events have similar values of $E_{\text{jet,K}}$ for a wide jet component. For a narrow jet component, the collimation-corrected kinetic energy of GRB 221009A is about an order of magnitude larger than that of the other VHE gamma-ray events, which may suggest that GRB 221009A has the largest isotropic-equivalent gamma-ray energy of the prompt emission among the known VHE GRBs. For all VHE gamma-ray events, the radio fluxes were observed, where they showed the difficulty for the standard afterglow model in explaining VHE gamma-ray and radio afterglows simultaneously. However, the two-component jet model could describe such complicated multiwavelength light curves from radio to VHE gamma-ray bands (Sato et al. 2023). Our result indicates that VHE gamma-ray events may commonly consist of a structured jet that can be resembled by two jet components with different angular sizes and bulk Lorentz factors.

ACKNOWLEDGMENTS

We thank Katsuaki Asano, Shigeo S. Kimura, and Shuta J. Tanaka for valuable comments. We also thank the anonymous referee for his/her/their helpful comments to improve the paper. This research was partially supported by JSPS KAKENHI Grant Nos. 22J20105 (Y.S.), 20H01901 (K.M.), 20H05852 (K.M.), 19H01893 (Y.O.), 21H04487 (Y.O.), and 22H01251 (R.Y.). The work of K.M. is supported by the NSF Grant Nos. AST-1908689, AST-2108466 and AST-2108467.

DATA AVAILABILITY

The theoretical model data underlying this article will be shared on reasonable request to the corresponding author.

REFERENCES

Abdalla H., et al. 2019, *Natur*, 575, 464
 Atteia J.-L., et al. 2017, *ApJ*, 837, 119
 Ayala H., HAWC Collaboration, 2022, *GCN*, 32683
 Berger E., et al., 2003, *Natur*, 426, 154
 Blanch O., MAGIC Collaboration, 2020, *ATel*, 14275
 Burns E., et al., 2023, *arXiv:2302.14037*
 Castro-Tirado A. J., et al., 2022, *GCN*, 32686
 Evans P. A., et al., 2007, *A&A*, 469, 379
 Evans P. A., et al., 2009, *MNRAS*, 397, 1177

Finke J. D., Razzaque S., Dermer C. D., 2010, *ApJ*, 712, 238
 Fraija N., et al. 2020, *ApJ*, 905, 112
 Franceschini A., Rodighiero G., Vaccari M., 2008, *A&A*, 487, 837
 Frederiks D., et al., 2023, *arXiv:2302.13383*
 Fulton M. D., et al., 2023, *arXiv:2301.11170*
 Gao H., et al., 2013, *NewAR*, 57, 141
 Gill R., Granot J., 2022, *Galax*, 10, 74
 Gilmore R. C., et al., 2012, *MNRAS*, 422, 3189
 Granot J., Piran T., Sari R., 1999, *ApJ*, 513, 679
 H.E.S.S. Collaboration 2021, *Sci*, 372, 1081
 Huang Y. F., et al., 2000, *ApJ*, 543, 90
 Huang Y. F., et al., 2004, *ApJ*, 605, 300
 Huang, Y., et al., 2022, *GCN*, 32677
 Jacovich T. E., Beniamini P., van der Horst A. J., 2021, *MNRAS*, 504, 528
 Kann D. A., et al, 2023, *arXiv:2302.06225*
 Laskar T., et al., 2023, *arXiv: 2302.04388*
 Levan A. J., et al., 2023, *arXiv: 2302.07761*
 Li T.-P., Ma Y.-Q., 1983, *ApJ*, 272, 317
 Ma X.-H., et al., 2022, *ChPhC*, 46, 030001
 MAGIC Collaboration, 2019a, *Natur*, 575, 455
 MAGIC Collaboration, 2019b, *Natur*, 575, 459
 Malesani D. B., et al., 2023, *arXiv:2302.07891*
 Murase K. et al., 2007, *ApJ*, 671, 1886
 Murase K. et al., 2010, *MNRAS*, 402, L54
 Murase K., et al., 2011, *ApJ*, 732, 77
 Murase K. et al. 2022, *ApJL*, 941, L10
 Nakar E., Ando S., Sari R., 2009, *ApJ*, 703, 675
 Nava L., 2021, *Univ*, 7, 503.
 O'Connor B., et al., 2023, *arXiv:2302.07906*
 Peng F., Königl A., Granot J., 2005, *ApJ*, 626, 966
 Pillera R., et al., Fermi-LAT team, 2022, *GCN*, 32658
 Racusin J. L., et al., 2008, *Natur*, 455, 183
 Ramirez-Ruiz E., Celotti A., Rees M. J., 2002, *MNRAS*, 337, 1349
 Ren J., Wang Y., Zhang L.-L., 2022, *arXiv:2210.10673*
 Rhodes L., et al., 2020, *MNRAS*, 496, 3326
 Rhodes L., et al., 2022, *MNRAS*, 513, 1895
 Ror A. K., et al., 2022, *arXiv:2211.10036*
 Sari R., Piran T., Halpern J. P., 1999, *ApJL*, 519, L17
 Sari R., Esin A. A., 2001, *ApJ*, 548, 787
 Sato Y., et al., 2021, *MNRAS*, 504, 5647
 Sato Y., et al., 2023, *JHEAp*, 37, 51
 Shrestha M., et al., 2023, *arXiv:2302.03829*
 Svensson, R., 1987, *MNRAS*, 227, 403
 Wang X.-Y., et al., 2010, *ApJ*, 712, 1232
 Wang X.-Y., et al., 2022, *ChPhC*, 46, 030003
 Williams M. A., et al., 2023, *arXiv:2302.03642*
 Wu X. F., et al., 2005, *MNRAS*, 357, 1197
 Zhang B. T., et al., 2021, *ApJ*, 920, 55
 Zhang B. T., et al. 2022, *arXiv:2211.05754*
 Zhao W., et al., 2020, *ApJ*, 900, 112

APPENDIX A: ONLINE MATERIAL

Enlarged view of Fig. 2 in the radio bands (1.3, 5.0, 15.8 and 99.9 GHz) is shown in Fig. A1.

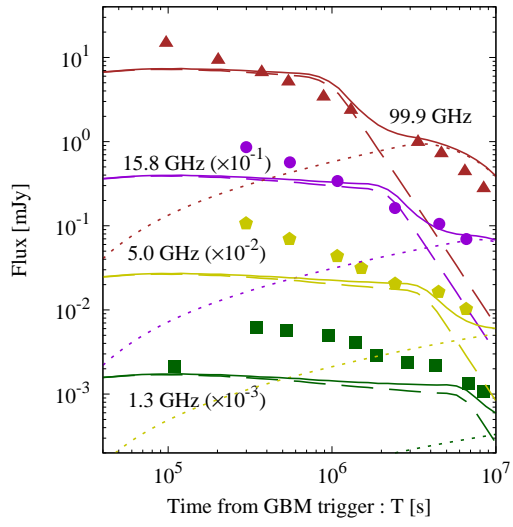


Figure A1. Enlarged view of Fig. 2 in the radio bands (1.3, 5.0, 15.8 and 99.9 GHz).